

Automated Image Analysis for 3D Tumor Coculture Spheroids

**Borbála Gergics^{1,2*}, Lilla Kisbenedek^{1,2}, András Füredi^{1,3},
Levente Kovács¹, and Dániel András Drexler¹**

¹Physiological Controls Research Center, University Research and Innovation Center, Obuda University, Bécsi út 96/b, 1034 Budapest, Hungary, {gergics.borbala, kisbenedek.lilla, furedi.andras, kovacs, drexler.daniel}@uni-obuda.hu

²Applied Informatics and Applied Mathematics Doctoral School, Obuda University, Bécsi út 96/b, 1034 Budapest, Hungary

³Drug Resistance Research Group, Hungarian Research Network, Magyar tudósok krt 2, 1117 Budapest, Hungary, furedi.andras@ttk.hu

*Corresponding: gergics.borbala@uni-obuda.hu

Abstract: Understanding the dynamics of the tumor microenvironment (TME) is essential for developing effective cancer therapies. Our primary aim is to establish improved mathematical models based on in vitro measurements to better characterize tumor behavior and microenvironmental interactions, and ultimately to bridge the gap between in vitro and in vivo systems. A prerequisite for such modeling is the quantitative assessment of structural changes in the tumor microenvironment. In this study, we employ 3D coculture spheroids consisting of CST tumor cells and 3T3 fibroblasts, treated with varying concentrations of doxorubicin. To facilitate accurate and automated analysis, we developed a Python-based image processing algorithm that extracts area and volume estimates from both fluorescent and brightfield microscopy images. These quantitative data provide insights into treatment response and enable dynamic modeling of tumor-stroma interactions. The proposed pipeline enhances reproducibility and scalability of in vitro studies and supports the construction of mechanistic models that reflect TME complexity.

Keywords: tumor modeling; tumor spheroid; image processing

1 Introduction

The tumor microenvironment (TME) is a complex and dynamic network of cells, signaling molecules (e.g., chemokines and cytokines), and structural components surrounding and interacting with tumor cells [1]. It plays a crucial role in cancer progression, influencing tumor growth, invasion, metastasis, and response to therapy [2–6]. Traditional two-dimensional (2D) cell culture models often fail to recapitulate the complex architecture and cellular interactions present *in vivo*.

In contrast, three-dimensional (3D) *in vitro* tumor models have emerged as more physiologically relevant systems, better mimicking the structural and functional complexities of the native tumors [7–9].

Fibroblasts, particularly cancer-associated fibroblasts (CAFs), are integral components of the TME. These cells are activated forms of stromal fibroblasts that transform in response to the tumor environment and actively support tumor growth, survival, and metastatic potential. They contribute to tumor progression by remodeling the extracellular matrix, secreting growth factors, and modulating immune responses. In addition, CAFs can help tumor cells to fend off the effects of drugs [10, 11]. Coculture of tumor cells with fibroblasts in 3D models has been shown to induce cancer-relevant pathways, improving our understanding of tumor-stroma interactions [12].

Mathematical modeling serves as a powerful tool to analyze and predict tumor behavior within the TME. By integrating experimental data from 3D coculture systems, models can simulate tumor growth dynamics, drug diffusion, and cellular interactions. Such models are instrumental in optimizing chemotherapy strategies, allowing for the prediction of treatment outcomes and the identification of potential therapeutic targets [13, 14]. The data required for mathematical modeling in the case of *in vitro* spheroid cocultures are based on microscopic images. Therefore, the analysis of microscopic images is a critical step in obtaining high-quality data. The analysis of images of 3D tumor spheroids and fibroblast cocultures faces several technical and methodological challenges [15]. For example, the size and density of spheroids limit the penetration of light, making it difficult to visualize internal structures using conventional microscopy techniques. Optical limitations include the fact that we see only a two-dimensional projection of a 3D structure. The size and morphology of spheroids can change during the experiment, making it difficult to automate image processing and comparative analyses [8, 16, 17]. In addition, many algorithms cannot adequately handle the complex morphology of spheroids, especially for non-compact or partially disintegrated structures. However, manual segmentation of large amounts of images is extremely time-consuming and subjective, which can affect the reproducibility of the results [18]. To overcome these challenges, it is essential to apply advanced image processing methods and algorithms, as well as to optimize microscopy techniques by taking into account the specificities of 3D spheroid models. There are many software and algorithms for analyzing microscopic images, some of which stand out for the study of 3D spheroids. Fiji/ImageJ is an open-source platform that allows for image segmentation, morphometric analysis, and quantitative evaluation with the help of several plugins [19]. CellProfiler is an automated image analysis software that is suitable for high-throughput image processing and quantification of various cell morphological features [20].

Advanced image segmentation techniques are widely spread techniques for accurately analyzing 3D tumor spheroids. Deep learning models such as UNet and HRNet have demonstrated high accuracy in segmenting both treated and untreated spheroids [21]. Open-source tools like SpheroidJ also offer adaptable algorithms for spheroid segmentation across diverse experimental settings [22]. Additionally,

soft computing methods like the Teaching–Learning–Based Optimization (TLBO) algorithm have proven effective in color-based segmentation, facilitating the distinction of different cell types in coculture systems [23]. OrganoSeg is an open-source image analysis algorithm specifically developed for the automated segmentation and quantification of organoid and spheroid structures in microscopy images. It applies thresholding and morphological operations to delineate object boundaries and extract quantitative features, such as area, shape, and intensity. Due to its robustness and ease of use, OrganoSeg has become a widely applied tool in high-throughput organoid and spheroid research [24]. While these techniques have shown high accuracy in specific experimental setups, their performance can vary significantly across different microscopy datasets. This variability arises due to differences in imaging conditions, sample preparation, and biological heterogeneity, making it challenging to generalize these algorithms without extensive customization.

In this study, we developed a workflow that integrates image analysis and preprocessing techniques to process 3D spheroid images effectively. This workflow serves as a foundational step toward constructing mathematical models that combine 3D *in vitro* coculture systems of tumor cells with computational simulations. The primary goal of these models is to elucidate the complex interactions within the tumor microenvironment (TME) and to utilize these insights for optimizing chemotherapy regimens. In Section 2, we summarize our previous work, then in Section 3 we detail the experimental setup, the applied image processing techniques, and the created workflow. In Section 4, we summarize and evaluate all the presented spheroid results based on the image detection. Additionally, we compare our algorithm to the previously mentioned OrganoSeg algorithm to validate its effectiveness. Finally, we highlight our contribution and summarize the current limitations of the algorithm.

2 Preliminaries

Based on our previous work, we found that the evaluation and automation of microscopic images of tumor spheroids is a complex and challenging process. In earlier studies, we used the JuLI™ STAT image analysis software, which is integrated with the JuLI™ Stage live-cell imaging system [25]. This software allows for basic image editing and thresholding, facilitating the determination of spheroid diameter and its relative size compared to the image frame. However, the automation of image analysis proved to be highly problematic. Manual evaluation of individual images becomes extremely time-consuming when processing larger datasets.

Furthermore, during cytotoxicity assays, the morphology of the spheroids changed significantly — spheroids tended to disintegrate into cellular debris, making it difficult to distinguish viable cells from dead material [26]. This greatly distorted the analytical results. A known characteristic of spheroids is the formation of a necrotic

core in the center, which contains non-viable cell remnants. Improper identification of this region can lead to inaccurate estimations of spheroid volume [27].

In our prior works, we attempted to mathematically model non-drug-induced necrotic effects (e.g., caused by nutrient or oxygen deprivation), as well as phototoxic effects arising from prolonged exposure to excitation light during fluorescence microscopy. However, these approaches did not yield satisfactory or broadly applicable results. The complexity increases further in coculture systems, where two distinct cell types must be evaluated simultaneously, particularly when assessing differential responses to chemotherapeutic agents [28, 29].

The aim of the present study is to develop an image processing algorithm capable of reliably analyzing the microscopic images generated during our cytotoxicity assays. This algorithm is intended to function automatically and consistently across various spheroid models used in our experiments.

3 Methods

3.1 Cell Cultures and Spheroid Formation

The tumor cell line used in this investigation originates from mammary tumors of genetically modified mice deficient in the *Bracl* and *p53* genes. This cell line is named CST. The Drug Resistance Research Group at the HUN-REN Research Center for Natural Sciences developed and maintained this cell line as a stable culture. CST cells were grown in cell culture flasks with 5 ml of specific medium (89% DMEM/F12, 10% FBS, 1% Penicillin-Streptomycin). The flask was incubated at 37 °C, 5% CO_2 and 95% humidity. Cell passaging was used when the cell culture became confluent [30].

The other cell line in the coculture was the 3T3 cell line, which is a type of immortalized mouse embryonic fibroblast cell line from the collection of the Drug Resistance Research Group at the HUN-REN Research Center for Natural Sciences. The 3T3 cells were grown in completed DMEM (10 % fetal bovine serum) in 37°C, 5% CO_2 , and 95% humidity.

For spheroid formation, a single cell suspension of CST tumor cells and 3T3 fibroblasts was seeded into a 96-well U-bottom microplate with a cell-repellent surface (Greiner BIO-ONE CELLSTAR), with a total initial cell number of 20000 cells/well. The cells were incubated for two days (37°C, 5% CO_2 and 95% humidity) and they aggregated into a single spheroid in one well spontaneously.

Spheroids with different ratios of tumor cells and fibroblasts were investigated: 1 part tumor and 1 part fibroblast (two parallel measurements, columns 2-3), 2 parts tumor and 1 part fibroblast (two parallel measurements, columns 4-5) and 1 part tumor and 2 parts fibroblast (two parallel measurements, columns 10-11). Figure 1 illustrates a schematic figure of the layout of the 96-well plate used in this experiment.

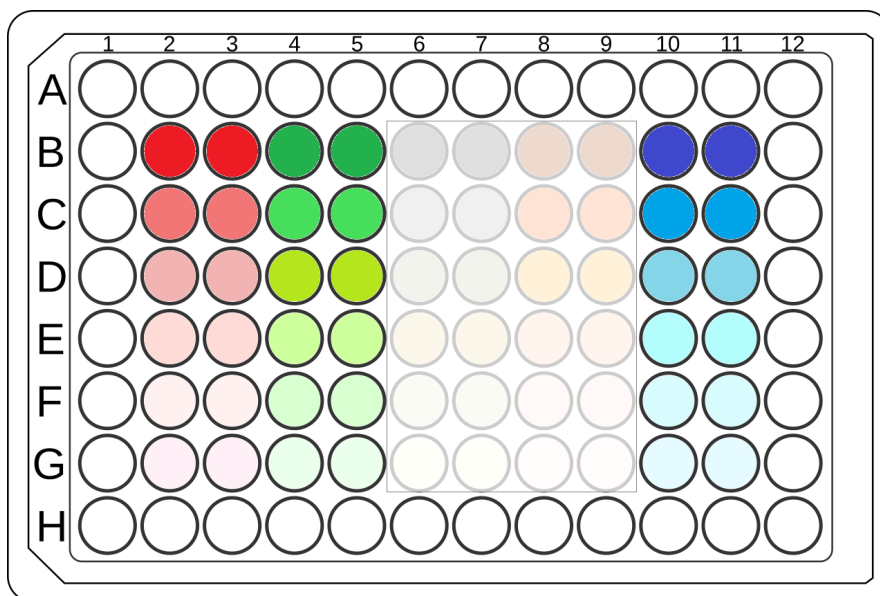


Figure 1

Schematic layout of the 96-well plate showing spheroids with varying tumor-to-fibroblast ratios and doxorubicin concentrations. The red columns (columns 2-3) contained spheroids with a 1:1 tumor:fibroblast ratio, the green columns (columns 4-5) contained spheroids with a 2:1 tumor:fibroblast ratio, while the blue columns (columns 10-11) contained spheroids with a 1:2 tumor:fibroblast ratio. Columns 6-7 and 8-9 contained spheroids with a 3:1 and 4:1 tumor:fibroblast ratio, but the evaluation of the images taken from these was omitted within the scope of this study. Rows B, C, D, E, F, G for each column contained spheroids treated with 10, 7.52, 5.65, 4.25, 3.2, and 0 μM doxorubicin, respectively.

3.2 Cytotoxicity Measurements

For cytotoxicity measurements, cells were treated with 6 different concentrations of doxorubicin solution (10, 7.52, 5.65, 4.25, 3.20, 0 μM , Figure 1) for 5 days. The drug was added at the beginning of the experiment, and it was not depleted from the wells. An automated microscope (JuLI™ Stage Cell History Recorder) was used to make images of spheroids every five hours. There were 25 time instants in total for each spheroid.

The CST tumor cell gene contains a gene for the red fluorescent protein mCherry (RFP), so when excited by light of a certain wavelength (587 nm), they fluoresce with red light and can therefore be detected using a fluorescent microscope.

However, 3T3 fibroblasts do not contain a fluorescent protein gene, so we took images of them in transmitted light (brightfield) using the automated microscope. The fluorescent and brightfield images were taken simultaneously, so that one fluorescent red and one brightfield image were taken of each spheroid at each measurement point. The fluorescent red images, therefore, show only the tumor cells, while the brightfield images show the projection of the entire spheroid

consisting of CST tumor cells and 3T3 fibroblasts.

We applied a 10x objective lens and took 3x3 images of the center of each well, which were stitched. The stitched images went through image analysis.

3.3 Image Analysis

We implemented a deterministic image-analysis pipeline in Python to quantify (i) tumor area from RFP-channel images and (ii) spheroid area and boundary geometry from brightfield (BF) images.

Figure 2 shows a representative output for spheroid B4 (2:1 tumor:fibroblast coculture, 10 μ M doxorubicin). The assay ran for 5 days with images acquired every 5 h (25 time points from 0 h to 120 h). Three time points are shown: 0 h, 60 h, and 120 h. The first column displays the RFP channel with suprathreshold signal overlaid in red, highlighting viable tumor regions. The second column shows the brightfield image with the spheroid boundary delineated in purple. The third column merges these views. In this example, the viable-tumor area remains approximately constant, whereas the total spheroid area expands and then returns toward its initial size. While the current implementation focuses on area changes, intensity variations are also informative; the algorithm can be easily extended to incorporate intensity-based metrics alongside area.

RFP (Tumor) Segmentation

Here we describe the pipeline used to produce the viable-tumor overlays shown in the first column of Figure 2.

Let $I_{\text{RFP}} \in \{0, \dots, 255\}^{H \times W}$ denote the 8-bit, single-channel RFP image. We index pixels as (y, x) with $y \in \{0, \dots, H - 1\}$ and $x \in \{0, \dots, W - 1\}$. We then convert the image to grayscale. To enable comparability over time and across different wells, we normalize intensities to $[0, 1]$ using fixed global bounds $I_{\text{min}} = 87.75$ and $I_{\text{max}} = 255$:

$$I^* = \frac{I_{\text{RFP}} - I_{\text{min}}}{I_{\text{max}} - I_{\text{min}}}. \quad (1)$$

A fixed threshold $T = 0.35$ (chosen from the first time point of the first image processed and then held constant) selects candidate tumor pixels:

$$M_{\text{raw}} = \{(x, y) : I^*(x, y) > T\}. \quad (2)$$

Then, it is cleaned by hole filling and 8-connected small-object removal (area cutoff 180 px), yielding M_{clean} .

Independently, to suppress saturated highlights attributable to veiling glare (e.g., residual out-of-focus fluorescence and internal reflections/excitation leakage in the optical train), we exclude the extreme upper tail of the normalized intensities:

$$M_{\text{back}} = \{(x, y) \mid I^*(x, y) \geq T_{\text{back}}\}, \quad (3)$$

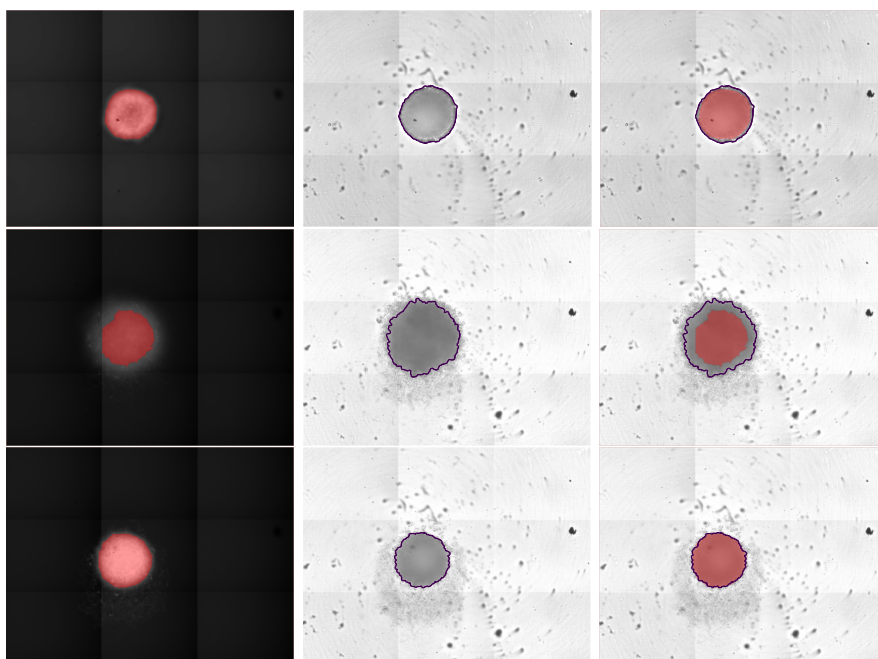


Figure 2

Automated segmentation of a tumor–fibroblast spheroid from spheroid B4 (2:1 ratio, $10\mu\text{M}$ doxorubicin) at three time points (0, 60, and 120 h). Rows correspond to time points. Columns show, from left to right: (i) RFP images with the tumor mask overlaid in red, (ii) brightfield images with the spheroid boundary delineated (purple), and (iii) a composite view illustrating spatial correspondence between channels.

where $T_{\text{back}} = 0.999$, which is an empirically set threshold.

We report M_{clean} as the segmentation mask, and compute tumor area by subtracting the number of glare pixels (counted over the whole image) from the number of pixels in M_{clean} :

$$A_{\text{tumor}} = |M_{\text{clean}}| - |M_{\text{back}}|. \quad (4)$$

If $A_{\text{tumor}} = 0$, we record NaN to denote no detectable tumor signal under the chosen threshold.

Brightfield Image Processing and Boundary Extraction

Here, we detail the spheroid boundary detection pipeline illustrated in the second column of Figure 2. Its processing main stages are shown in Figure 3, arranged left-to-right and top-to-bottom.

Brightfield images (I_{BF}) are loaded as RGB (alpha, if present, is discarded) and converted to grayscale. We apply a per-image contrast stretch using the 2.5 and 97.5 intensity percentiles. These values are empirically adjusted. This contrast stretch can be described as:

$$\tilde{I} = \left(\frac{I_{\text{BF}} - p_{2.5}}{p_{97.5} - p_{2.5}} \right). \quad (5)$$

We convolve \tilde{I} with a Gaussian filter ($\sigma_g = 1.0$), where σ sets the smoothing scale: larger σ_g more strongly suppresses high-frequency speckle, while smaller σ preserves fine detail but passes more noise. We then threshold the smoothed image at level $\alpha = 0.3$ to obtain a binary mask. This low threshold is intended only for coarse background suppression and removal of obvious artifacts, not for final segmentation. After removing small holes and objects (threshold = 180 px) with `skimage.morphology`, we label connected components `skimage.measure` and retain only the largest component as the putative spheroid-covered region. To obtain a clean boundary, we detect edges with the Canny algorithm (`skimage.feature.canny`, $\sigma_c = 1.5$), then bridge small gaps via binary closing (`skimage.morphology.binary_closing`). After that, we use a disk structuring element of radius 10 px, and discarded residual edge fragments by removing connected components smaller than 180 px. We pad the edge image by 10 px on all sides and fill enclosed holes to obtain a filled region. In order to avoid counting the 1-pixel edge itself, we subtract the edge from the filled region, re-label connected components, and retain the largest interior component - the final area in pixels. For visualization and downstream shape analysis, we recompute the binary Canny edge on the image again and use it as the final boundary on the images.

Circle Detection (Hough Transform)

Quantifying volume is essential for mechanistic modeling. To relate *in vitro* spheroid measurements to *in vivo* tumor volumes, we usually need to estimate a 3D volume from 2D images. We currently assume approximate spherical symmetry: we

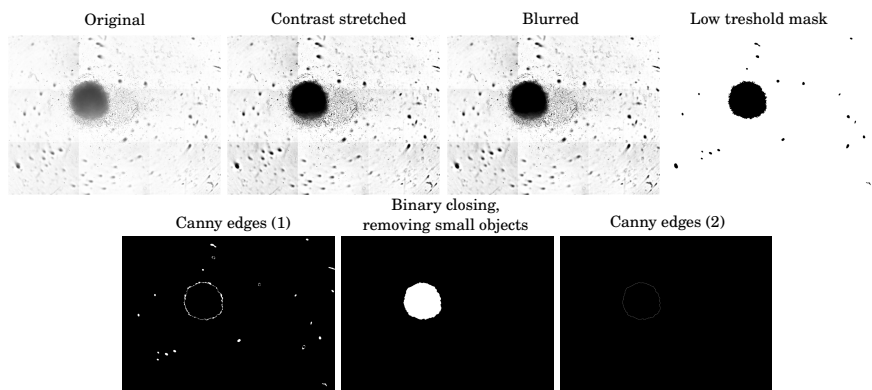


Figure 3

The main stages of spheroid edge detection in case of the D2 spheroid 6th measurement (30 h).

fit a circle to the detected (approximately circular) spheroid boundary and compute $V \approx \frac{4}{3}\pi r^3$ (with r in pixels, convertible to physical units via the pixel size).

We apply a circular Hough transform to the final binary edge map over radii $r \in [180, 500]$ px in 15 px increments, and retain the single strongest accumulator peak. This yields the center (c_x, c_y) and radius r^* when a peak is found, otherwise we no circle detected. Figure 4 illustrates a representative case (spheroid D2, 30 h): the left panel shows the brightfield image with the detected circle overlaid in red, and the right panel shows the corresponding Hough accumulator.

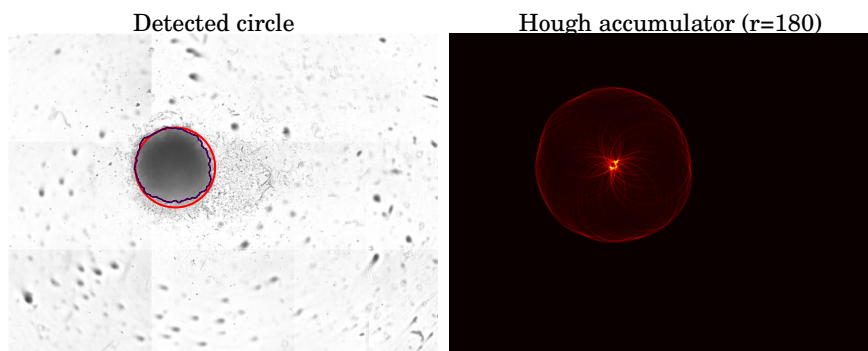


Figure 4

Circle detection for spheroid D2 (6th measurement (30 h)). The left figure shows the brightfield image with the detected circle. The right figure visualizes the Hough accumulator, i.e., the vote map of the circular Hough transform.

4 Results

We applied our image processing workflow to quantify spheroid volume dynamics over a five-day cytotoxicity assay using cocultures of CST tumor cells and 3T3 fibroblasts exposed to varying concentrations of doxorubicin. Figure 5 shows the temporal evolution of both fluorescent (RFP) (first column of 5) and brightfield (second column of 5) area of the microscopic images across three experimental groups (1:1, 2:1 and 1:2 tumor:fibroblast ratios, detailed in Subsection 3.1). The red, green, and blue curves represent groups of spheroids with different ratios, respectively. The color intensity increases with the concentration of doxorubicin. This color coding is the same as in Figure 1.

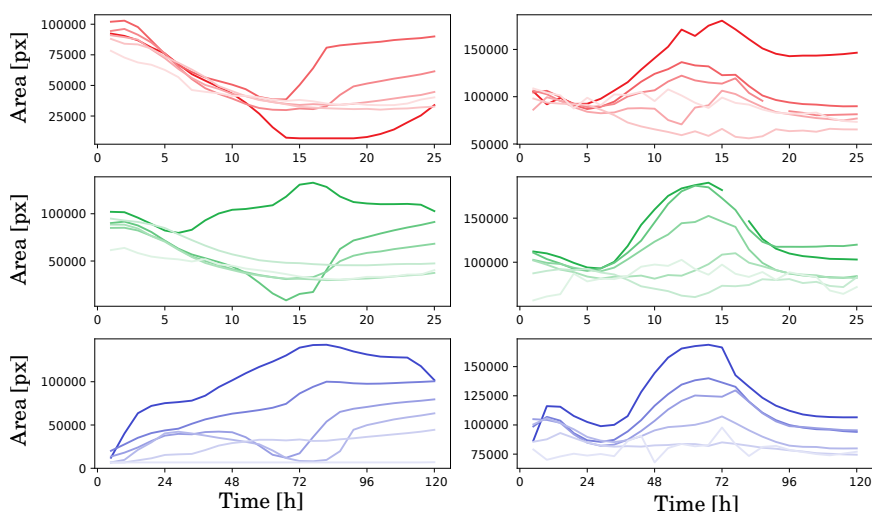


Figure 5

Results of image analysis. The first column shows the temporal distribution of the red fluorescent area of the fluorescence microscopic images. The second column shows the temporal change in the area of the spheroids segmented from the brightfield microscopic images. The red curves represent the groups of spheroids with a 1:1, the green curves represent the 2:1, and the blue curves represent the groups of spheroids with a 1:2 tumor:fibroblast ratio. Increasing concentrations of doxorubicin are indicated by increasing color intensity of curves.

In all groups, we observed a consistent decrease in both RFP and brightfield areas with increasing drug concentration, indicating a dose-dependent cytotoxic effect. The RFP-based areas — representing tumor cell mass — tended to decrease more rapidly than brightfield areas, which supports that doxorubicin has less effect on fibroblasts than on tumor cells [31, 32]. Brightfield-derived measurements, encompassing both tumor and fibroblast components, remained relatively larger, especially at lower drug doses.

Notably, columns 10-11 (higher fibroblast ratio) exhibited delayed and attenuated area reduction compared to groups with 1:1 and 2:1 tumor:fibroblast ratios, suggesting a possible protective effect of fibroblasts against doxorubicin-induced

cytotoxicity [32, 33]. This supports the hypothesis that stromal composition significantly modulates treatment response, highlighting the importance of tumor microenvironment interactions in therapeutic evaluation.

For validation of the effectiveness of the developed image analysis algorithm, we compared the segmentation results with a well-functioning, reliable method, called OrganoSeg [24]. Figure 6 shows the segmentation results of the two methods for the 1:2 ratio group for all 6 drug concentrations (Figure 1, column 10, wells B-G). Each subplot shows the temporal changes of the areas segmented by two different methods in a brightfield microscopic image of the given spheroid. Spheroid areas were computed using an area calibration of $0.6684^2 \mu\text{m}^2$ per pixel, multiplying the pixel counts accordingly. The dotted curves represent the results of the analysis performed with OrganoSeg, while the smooth curves represent the results of the analysis performed with our algorithms.

The results indicate that our algorithm consistently identified smaller segmented areas compared to OrganoSeg, however, the overall trends of the resulting curves were comparable across both methods, supporting the validity of our algorithm. Both software recognize the boundaries of tumor spheroids and their alteration in a comparable way. The main difference is that the software we developed can segment a larger amount of microscopic images in a significantly reduced timespan, thereby saving time, which is especially important when processing longitudinal measurements for proper mathematical modeling and parameter estimation.

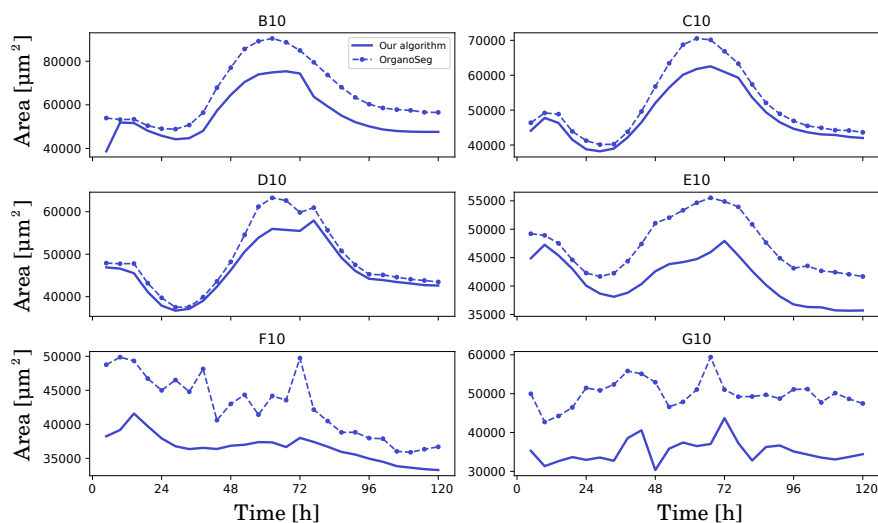


Figure 6

Comparison of our algorithm and OrganoSeg. The individual subplots depict the temporal change of the segmented areas from brightfield microscopy images of the marked spheroids. The dotted curves show the results of the segmentation performed with OrganoSeg, while the smooth curves show the results of the segmentation performed with our algorithm.

In future applications, the two methods should be used in a complementary workflow: run our fast pipeline by default for most images, and escalate only the minority cases to OrganoSeg under supervision for refinement. This workflow preserves accuracy while substantially reducing hands-on analysis time.

Conclusions

In this study, we presented an automated image analysis workflow designed to quantify volumetric changes in 3D tumor–fibroblast coculture spheroids during chemotherapy treatment. By integrating brightfield and fluorescent imaging with Python-based segmentation routines, we were able to extract dynamic quantitative data that reflect different treatment responses across varying fibroblast-to-tumor ratios. Our results confirm the potential protective role of fibroblasts in modulating doxorubicin sensitivity, reinforcing the importance of the tumor microenvironment in therapeutic outcomes. Although the current algorithm has limitations in robustness and accuracy under certain conditions, it provides a scalable and reproducible foundation for supporting mechanistic *in vitro–in vivo* modeling. Future improvements will focus on enhancing segmentation accuracy and incorporating these quantitative outputs into predictive mathematical models of tumor response.

Acknowledgment

This project has been supported by the Hungarian National Research, Development and Innovation Fund of Hungary, financed under the TKP2021-NKTA-36 funding scheme. The work of Dr. Dániel András Drexler was supported by the Starting Excellence Researcher Program of Obuda University, Budapest, Hungary. Borbála Gergics was supported by the 2024-2.1.1 University Research Scholarship Program of the Ministry for Culture and Innovation from the source of the National Research, Development and Innovation Fund. This research was partially supported by the European Union (EU HORIZON-MSCA-2023-SE-01-01) and the Hungarian NRDI program (2020-2.1.1-ED-2024-00346) within the DSYREKI: Dynamical Systems and Reaction Kinetics Networks project.

References

- [1] D. Wirtz, K. Konstantopoulos, and P. C. Searson. The physics of cancer: the role of physical interactions and mechanical forces in metastasis. *Nature Reviews Cancer*, 11(7):512–522, 2011.
- [2] B. Arneth. Tumor microenvironment. *Medicina*, 56(1):15, 2019.
- [3] N. M. Anderson and M. C. Simon. The tumor microenvironment. *Current Biology*, 30(16):R921–R925, 2020.
- [4] F. R. Balkwill, M. Capasso, and T. Hagemann. The tumor microenvironment at a glance. *Journal of Cell Science*, 125(23):5591–5596, 2012.

- [5] T. Whiteside. The tumor microenvironment and its role in promoting tumor growth. *Oncogene*, 27(45):5904–5912, 2008.
- [6] T. Wu and Y. Dai. Tumor microenvironment and therapeutic response. *Cancer Letters*, 387:61–68, 2017.
- [7] G. Lazzari, V. Nicolas, M. Matsusaki, M. Akashi, P. Couvreur, and S. Mura. Multicellular spheroid based on a triple co-culture: A novel 3d model to mimic pancreatic tumor complexity. *Acta Biomaterialia*, 78:296–307, 2018.
- [8] J.-H. Lee, S.-K. Kim, I. A. Khawar, S.-Y. Jeong, S. Chung, and H.-J. Kuh. Microfluidic co-culture of pancreatic tumor spheroids with stellate cells as a novel 3d model for investigation of stroma-mediated cell motility and drug resistance. *Journal of Experimental & Clinical Cancer Research*, 37:1–12, 2018.
- [9] T. Liu, B. Lin, and J. Qin. Carcinoma-associated fibroblasts promoted tumor spheroid invasion on a microfluidic 3d co-culture device. *Lab on a Chip*, 10(13):1671–1677, 2010.
- [10] P. Farmer, H. Bonnefoi, P. Anderle, D. Cameron, P. Wirapati, V. Bécette, S. André, M. Piccart, M. Campone, E. Brain, et al. A stroma-related gene signature predicts resistance to neoadjuvant chemotherapy in breast cancer. *Nature Medicine*, 15(1):68–74, 2009.
- [11] E. Sahai, I. Astsaturov, E. Cukierman, D. G. DeNardo, M. Egeblad, R. M. Evans, D. Fearon, F. R. Greten, S. R. Hingorani, T. Hunter, et al. A framework for advancing our understanding of cancer-associated fibroblasts. *Nature Reviews Cancer*, 20(3):174–186, 2020.
- [12] J. Mason and D. Öhlund. Key aspects for conception and construction of co-culture models of tumor-stroma interactions. *Frontiers in Bioengineering and Biotechnology*, 11:1150764, 2023.
- [13] R. J. Murphy, G. Gunasingh, N. K. Haass, and M. J. Simpson. Formation and growth of co-culture tumour spheroids: new compartment-based mathematical models and experiments. *Bulletin of Mathematical Biology*, 86(1):8, 2024.
- [14] B. Gergics, L. Kovács, and D. A. Drexler. Mathematical modeling of in vitro tumor spheroid co-cultures: a literature review. In *2025 IEEE 29th International Conference on Intelligent Engineering Systems (INES)*. in press, 2025.
- [15] W. Chen, C. Wong, E. Vosburgh, A. J. Levine, D. J. Foran, and E. Y. Xu. High-throughput image analysis of tumor spheroids: a user-friendly software application to measure the size of spheroids automatically and accurately. *Journal of Visualized Experiments: JoVE*, (89):51639, 2014.
- [16] A. Akshay, M. Katoch, M. Abedi, N. Shekarchizadeh, M. Besic, F. C. Burkhard, A. Bigger-Allen, R. M. Adam, K. Monastyrskaya, and A. H.

- Gheinani. Spheroscan: a user-friendly deep learning tool for spheroid image analysis. *GigaScience*, 12:giad082, 2023.
- [17] N. Dorst, M. Oberringer, U. Grässer, T. Pohlemann, and W. Metzger. Analysis of cellular composition of co-culture spheroids. *Annals of Anatomy-Anatomischer Anzeiger*, 196(5):303–311, 2014.
- [18] M. Boutros, F. Heigwer, and C. Laufer. Microscopy-based high-content screening. *Cell*, 163(6):1314–1325, 2015.
- [19] J. Schindelin, C. T. Rueden, M. C. Hiner, and K. W. Eliceiri. The imagej ecosystem: An open platform for biomedical image analysis. *Molecular Reproduction and Development*, 82(7-8):518–529, 2015.
- [20] A. E. Carpenter, T. R. Jones, M. R. Lamprecht, C. Clarke, I. H. Kang, O. Friman, D. A. Guertin, J. H. Chang, R. A. Lindquist, J. Moffat, et al. Cellprofiler: image analysis software for identifying and quantifying cell phenotypes. *Genome Biology*, 7:1–11, 2006.
- [21] M. Streller, S. Michlíková, W. Ciecior, K. Lönnecke, L. A. Kunz-Schughart, S. Lange, and A. Voss-Böhme. Image segmentation of treated and untreated tumor spheroids by fully convolutional networks. *GigaScience*, 14, 2025.
- [22] D. Lacalle, H. A. Castro-Abril, T. Randelovic, C. Domínguez, J. Heras, E. Mata, G. Mata, Y. Méndez, V. Pascual, and I. Ochoa. Spheroidj: An open-source set of tools for spheroid segmentation. *Computer Methods and Programs in Biomedicine*, 200:105837, March 2021.
- [23] M. Sharma, V. S. Goudar, M. P. Koduri, F. G. Tseng, and M. Bhattacharya. Quantitative and qualitative image analysis of in vitro co-culture 3d tumor spheroid model by employing image-processing techniques. *Applied Sciences*, 11(10):4636, May 2021.
- [24] M. A. Borten, S. S. Bajikar, N. Sasaki, H. Clevers, and K. A. Janes. Automated brightfield morphometry of 3d organoid populations by organoseg. *Scientific Reports*, 8(1):5319, 2018.
- [25] NanoEnTek. Juli™ stage real-time cell history recorder quick manual. http://www.julistage.com/support/Download/JuLI%20Stage%20Quick%20Manual_V.1.5.pdf. last accessed: August 15 2022.
- [26] V. Charwat, K. Schütze, W. Holnthoner, A. Lavrentieva, R. Gangnus, P. Hofbauer, C. Hoffmann, B. Angres, and C. Kasper. Potential and limitations of microscopy and raman spectroscopy for live-cell analysis of 3d cell cultures. *Journal of Biotechnology*, 205:70–81, 2015.
- [27] S. Breslin and L. O’Driscoll. Three-dimensional cell culture: the missing link in drug discovery. *Drug Discovery Today*, 18(5-6):240–249, 2013.
- [28] B. Gergics, F. Vajda, M. Puskás, A. Füredi, and D. A. Drexler. Mathematical modeling of phototoxicity during fluorescent imaging of tumor spheroids. In

- 2023 *IEEE 27th International Conference on Intelligent Engineering Systems (INES)*, pages 000291–000296. IEEE, 2023.
- [29] B. Gergics, F. Vajda, A. Ládi, A. Füredi, and D. A. Drexler. Pharmacodynamics modeling based on in vitro 3d cell culture experiments. In *2023 IEEE 17th International Symposium on Applied Computational Intelligence and Informatics (SACI)*, pages 000499–000504. IEEE, 2023.
- [30] L. Hátori, G. Kudlik, K. Szabéni, N. Kucsma, B. Szeder, Póti, F. Uher, G. Várady, D. Szüts, F. A. Tóvári, J., and G. Szakács. Establishment and characterization of a *brca1*^{-/-}, *p53*^{-/-} mouse mammary tumor cell line. *International Journal of Molecular Sciences*, 21:4, 2 2020.
- [31] D. K. Logsdon, G. F. Beeghly, and J. M. Munson. Chemoprotection across the tumor border: cancer cell response to doxorubicin depends on stromal fibroblast ratios and interstitial therapeutic transport. *Cellular and Molecular Bioengineering*, 10(5):463–481, 2017.
- [32] W. B. Fang, M. Yao, and N. Cheng. Priming cancer cells for drug resistance: role of the fibroblast niche. *Frontiers in Biology*, 9(2):114–126, 2014.
- [33] K. Harati, A. Daigeler, T. Hirsch, F. Jacobsen, B. Behr, C. Wallner, M. Lehnhardt, and M. Becerikli. Tumor-associated fibroblasts promote the proliferation and decrease the doxorubicin sensitivity of liposarcoma cells. *International Journal of Molecular Medicine*, 37(6):1535–1541, 2016.